Amorphous and crystalline phase formation during suspension plasma spraying of the alumina–zirconia composite

F. Tarasi [a], M. Medraj [a,*], A. Dolatabadi [a], J. Oberste-Berghaus [b,c], C. Moreau [b]

[a] *Mechanical Engineering Department, Concordia University, Montreal, Quebec, Canada*
[b] *National Research Council of Canada-Industrial Material Institute, Boucherville, Quebec, Canada*

Abstract

The focus of this study is the amorphous phase formation in the alumina–yttria stabilized zirconia composite coatings during thermal spray deposition. The investigated processes include conventional and suspension plasma spraying. The focus of this paper is on suspension spraying, while making a comparison of the two processes. Through the study of the in-flight collected particles and coatings produced from the two processes, the comparison of fragmentation, melting and mixing phenomena became possible. Scanning electron microscopy, differential scanning calorimetry and X-ray diffractometric studies helped better understanding of the formation and the nature of amorphous and crystalline phases within the as-sprayed coatings. The results support the importance of melting and mixing phenomena during spraying on the amorphous phase formation, so that longer exposure at high temperature (lower in-flight particle velocity) results in higher amorphous contents due to more complete melting and mixing. The comparison of the atmospheric and suspension plasma spray methods presents several similarities in terms of melting and mixing behaviour and the resulting phases. The two methods are, however, different in fragmentation and the eventual crystallite sizes. The formation of crystalline supersaturated solid solutions of alumina and zirconia in SPS coatings is confirmed.
© 2011 Elsevier Ltd. All rights reserved.

Keywords: Amorphous phases; Ceramic composite coating; X-ray diffraction (XRD); Suspension plasma spraying

1. Introduction

Alumina–yttria stabilized zirconia (alumina–YSZ) is an interesting potential alternative to the present YSZ thermal barrier coatings (TBCs).[1,2] TBCs are used to enhance the life time of parts exposed to high temperature during service. Presently, the most industrially used TBC is the yttria stabilized zirconia, which is commonly deposited by plasma spray processes. Atmospheric plasma spray (APS) is the conventional method; and suspension plasma spray (SPS) is a modification of APS process in which small feed powders are injected to the plasma jet using a liquid carrier.

The equilibrium phase diagram of the alumina–zirconia system is shown in Fig. 1. Fig. 1(a) shows that a eutectic transformation occurs at 1860 °C with a composition of about 58% alumina. Upon cooling the transformation of cubic zirconia

solid into tetragonal phase completes at eutectoid temperature of 2260 °C and transformation into monoclinic phase in the presence of alumina takes place at 1150 °C. In addition to phase transformation temperatures, Fig. 1(a) shows that alumina and zirconia have a complete miscibility in liquid state, while the solubility limit of alumina into solid zirconia is very low (less than 2%) and that of zirconia into solid alumina is nearly zero. The solubility of the zirconia into solid alumina, according to the equilibrium phase diagrams presented in some other references,[3] may extend to about 5%. Such limited solubility in solid state is known to maximize the possibility of amorphous phase formation during rapid solidification of the composite melt.[3]

In thermal spray processes, such as plasma spray, the slow cooling condition to reach equilibrium is unfeasible. Coatings are not expected to show the same structures as predicted by equilibrium phase diagram, because of the rapid solidification and non-equilibrium cooling rates during spray process. Conversely, some metastable structures might be observed in as-deposited composite coatings. In the meantime, it is important to know the phase composition of the as-sprayed coatings,
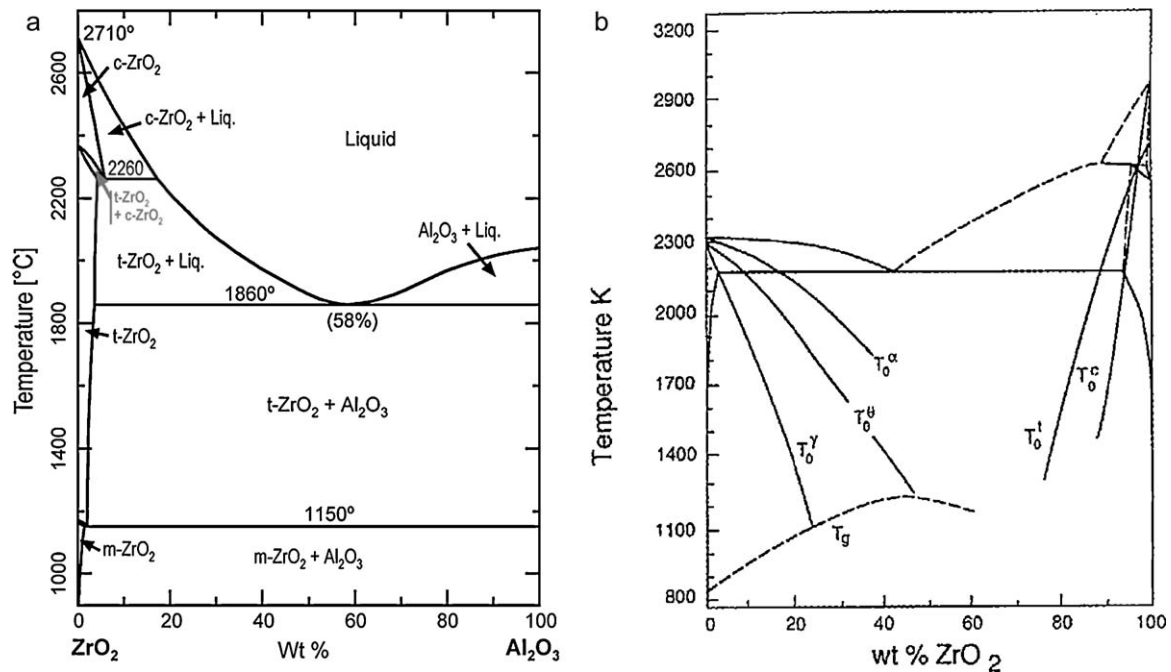
Fig. 1. (a) Binary equilibrium phase diagram of zirconia-alumina system[4] and (b) critical cooling curves superimposed on binary equilibrium phase diagram of alumina–zirconia system.[5]

since it determines their properties. In addition, these phases may undergo transformation upon heating and influence the eventual coating structure in service. Some of the possible non-equilibrium (metastable) phases in alumina–zirconia system can be found in Fig. 1(b) which is a superimposition of the critical cooling curves (for the formation of non-equilibrium phases) indicated by T_0 lines on the equilibrium phase diagram. Phases like γ- and θ-alumina or tetragonal and cubic zirconia are stable phases at higher temperatures and can be present in coatings at room temperature due to non-equilibrium cooling rates. In addition, this figure predicts the formation of glass (i.e. amorphous phases) at higher cooling rates when solidification happens at lower temperatures. T_g in this figure is the glass transition temperature which is maximum for eutectic composition. Therefore, it is expected that the eutectic composition gives rise to higher likelihood of amorphous phase formation.

Formation of amorphous phases is a notable feature of the as-sprayed coatings of composite materials such as alumina–zirconia. These phases, as mostly indivisible part of as-sprayed coatings, have not been well considered. Amorphous structure is normally formed as a result of rapid solidification. Fauchais et al.[5] reported cooling rates up to 600×10^6 K/s in the conventional plasma spray process using micron-sized particles. In addition, splat cooling rates in the order of 10^7 K/s[6] and 10^8 K/s[7] were reported by McDonald et al. during APS spraying, depending on the feed and substrate materials as well as the surface temperature and oxidation. In the SPS process which deals with much smaller particles, still larger cooling rates are conceivable. At such high cooling rates, the likelihood for ordering into crystalline structure during solidification from the melt

is greatly reduced. In composite systems with low solid solubility such as the current system, this effect is more severe because of a large atomic number and size difference between Al and Zr. In fact, there are reports of almost fully amorphous coatings during APS deposition of alumina-stabilized zirconia composite powders.[8,9]

Kim and Kim[8] sprayed alumina–zirconia with 42 wt% ZrO_2 stabilized with 2.3 wt% TiO_2 and 58 wt% Al_2O_3 by APS using micron-size powder and obtained a fully amorphous coating. Sodeoka et al.[10] reported the presence of the amorphous phase in 50/50 volume ratio of alumina/3YSZ (zirconia stabilized with 3 mol% yttria) spray dried nano-powders coated using the same process (APS). Vasiliev and Padture[11] reported a similar observation in the solution precursor plasma sprayed composite coating of alumina–zirconia in either binary composite[12] or ternary with yttria,[11] both with 10 and 20 mol% of alumina. They could observe the amorphous phase through transmission electron microscopy studies. Oberste-Berghaus et al.[13] sprayed both nano-powder and some comparatively larger particles (a few micron) of alumina–zirconia (zirconia was stabilized with 8 wt% yttria) using SPS process. They calculated the amorphous content based on the XRD pattern measurements. SPS coatings obtained from nano-particles presented no amorphous phase, while the amount of this phase for the larger particles was as high as 55 vol%. Amorphous phases, so frequently reported and sometimes observed as the dominant structure of the coatings, are worth more consideration in terms of the mechanisms of formation and their influence on the properties of the sprayed materials. The focus of this study is to identify the sources of the amorphous phase in the SPS process and provide a comparison of SPS with APS process in spraying the alumina-YSZ compos-

Table 1
Powder feed details.

Powder#	Powder mixture type	Feed powder mixture detail
1	Agglomerates of nano-particulates	Al_2O_3/3YSZ 60/40 (Tosoh, Grove City, OH, USA, 45 µm)
2	Loose nano-powders mixture	(8 mol% YSZ + 3 mol% YSZ) (both Inframat Advanced Materials, Farmington, USA; 30–60 nm) + Alumina (Nanoamor Advanced Ceramic Materials Inc., Houston, TX, USA; 23–47 nm)
3	Loose micron-powders mixture	8 mol% YSZ from (Unitec Norwal, CT, USA; average size 1.5 µm) + 3 mol% YSZ (Tosoh, Grove City, OH, USA; average size 2 µm) + Alumina 95% pure (Malakoff, TX, USA; average size 1.4 µm)
4	Nano 8 wt%YSZ mixture	(8 mol% YSZ + 3 mol% YSZ) (both Inframat Advanced Materials, Farmington, USA; 30–60 nm)

ite. This investigation aims at obtaining a better understanding of the formation and nature of the amorphous and crystalline phases in plasma spray coatings.

2. Materials and methods

To generate the coating samples, SPS process was used for deposition of powders with pseudo-eutectic composition of alumina–8 wt% YSZ, and one 8 wt% YSZ powder as the reference material. Powder mixtures with a weight ratio of 60/40 for alumina/8 wt% YSZ were produced in three different groups in terms of size range or morphology. Table 1 summarizes the details of the feed powders and the sprayed powder mixtures. Powder mixtures were suspended in ethanol with 30 wt% solid concentration. Suspension dispersion was done using 9cc poly-ethylene-emine and 4.5cc nitric acid, both with 10 wt% concentration, for every 150 g of solid. The suspensions were milled (ball milled in the case of micron-size powders) for 72 h at 90 RPM rotation speed for proper mixing. The suspensions were also magnetic-mixed during spray process to avoid settlement of the solid particles. In addition, powder#1 in Table 1 was also sprayed by atmospheric plasma spray process, i.e. in dry condition, using the same spray torch as used in SPS process. The spray condition for the APS spray is mentioned in Table 2. The in-flight particles from this process were collected into water for comparison with that resulted from the SPS process.

Mettech Axial III (Northwest Mettech, North Vancouver, Canada) was used to spray the suspensions on the substrates at a spray distance of 50 mm (as coatings) and into a water reservoir at 30–50 cm distance, to study the in-flight particles. A simplified schematic view of the spray system is shown in Fig. 2.

Atomization of the suspension was realized with two different methods. First one was by atomizing the suspension using a central tube passing through the liquid injection tube. This central tube was used for carrying the argon atomizing gas with a 6 slm flow rate. In addition, nitrogen shielding gas at 1 slm was transferred to the torch exit through the space between the injection tube and the nozzle. This system of injection and atomization using two gases is called "system 1" in this text. The second method was liquid injection without central gas carrying tube and just 14 slm nitrogen gas passing through the gap between the injection tube and the nozzle, called "system 2". The injection pressure of the suspension in both cases was about 30 psi. The substrates were (2.5 cm × 7.5 cm with 1.2 cm thickness) Inconel 625 (when system 1 was used) or mild steel (when system 2 was employed), both bond coated with about 200 µm NiCrAlY using high velocity oxyfule (HVOF) process. Different substrates were used for some characterization purposes out of this study.

System 1 was supposed to improve the deposition condition by reducing the clogging at the tip of the torch as well as to enhance melting by atomizing the droplets into smaller fragments. In practice, even though the jet stability looked better and the clogging was largely reduced, the fragmentation of the suspension jet, particle melting and coating qualities (integrity) were clearly better when system 2 was used. Details of the coating qualities and particle melting in both cases will follow. The spray and atomization conditions for each mixture, as well as the resulting particle velocity and temperature are indicated in Table 3. In this table the amorphous phase of the coatings was compared according to both, the differential scanning calorimetry (DSC) curves using a TG96 apparatus (Setaram Inc., Caluire, France) and the XRD results using Bruker D8-Discovery diffractometer (Bruker AXS, Inc., Madison, WI, USA). The DSC test includes incremental heating of the samples and measurement of the heat flux between the sample and a reference (here sapphire). The amount of the amorphous phase in the samples can be compared according to the area under the peak related to the crystallization heat release in the DSC curve. Since the areas under the curves do not represent the absolute values of the amorphous phases, the results are presented with arbitrary units. The amorphous phase in bond coated samples is calculated using XRD patterns of the coatings surfaces. This method is used to avoid the difficulties of detaching the coating from the substrate (which is required for the DSC test samples). The amorphous phase comparison with XRD patterns is based on the ratio of

Table 2
Atmospheric plasma spray conditions.

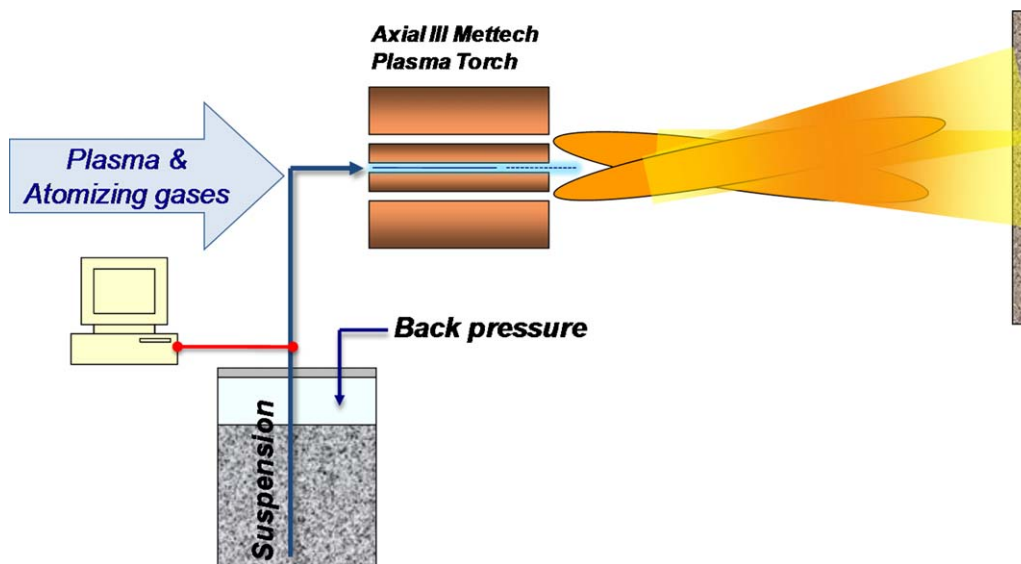| Total gas (slm)	Plasma current (A)	Gas composition (Ar/N_2/H_2)	Spray distance (µm)
120	200	10/80/10	100

Fig. 2. Schematic of the suspension plasma spray (SPS) system with axial injection.

the amorphous hump area to the total area under the peaks and humps. The two methods are more detailed elsewhere.[14]

The in-flight particle temperature and velocity are measured by AccuraSpray G2 (Tecnar Automation, St. Bruno, Canada). This is an optical diagnostic system collecting thermal radiation emitted from an ensemble of particles in the spray jet. The measurements are done in the center of the torch at the spray distance and are reported in Table 3 as T_p and V_p. The study of the morphology and chemical analysis using energy dispersive X-ray spectrometry (EDS) of the collected particles and coatings have been done using SEM (Hitachi S4700 GCEMarket, Inc., Blackwood, NJ, USA).

3. Results and discussion

3.1. Collected in-flight particles

As shown in Table 3, the measured crystallization peak area was minimum, i.e. 10 units, when system 1 was used for spraying powder#2 (loose nano-particles). This peak in the case of powder#1 (agglomerated nano-particulates) is slightly higher, equal to 12 units. The largest amount of amorphous phase is formed after spraying powder#3 (micron-size particles), with crystallization peak area as large as 28 units. However, using system 2 resulted in larger crystallization peak areas in both powders. Indeed, for sprayed powder#2, the peak area increased to 20 units and that of powder#3 was as large as 42 units. To investigate the reason for these differences, the micrographs of the collected particles, shown in Fig. 3(a)–(e), are used. In this figure, the different size and melting ratios of the porous aggregates of nano-powders in either loose or agglomerated conditions as compared with dense (non-porous) micron-particles are evident.

The reason for different behaviour of the nano- and micron-particles during the atomization process, including its dependence on the atomizing system and its interaction with the flame, are important subjects that require detailed study which is outside the scope of this work. However, the differences in melting and mixing behaviour observed in the current investigation helped to reveal the significance of these processes for amorphous formation. Investigating the effect of melting and mixing phenomena could explain why the in-flight particle velocity has played a role on the amount of these phases that could exceed the importance of the cooling rate.[14]

Collected particles of powder#3 (micron-powders) after spraying with systems 1 and 2, shown in Fig. 3(c) and (e) respectively, are clearly smaller than those of nano-powders in Fig. 3(a) and (b). This suggests their better treatment (in terms of heating, melting and shear forces on the molten droplet) by plasma flame resulting in more fragmentation in the suspension jet. In addition, the totally round shape of almost all of these particles (micron-size) indicates their extensive melting. Better heat treatment and melting in the plasma flame has resulted in larger fraction of amorphous phase in this powder type, which initially consisted of comparatively large and dense particles. The effect of applying system 2 for powder#2 can also be observed by comparing Fig. 3(b) and (d) in which better fragmentation and more melted round particles can be distinguished when system 2 is used.

Fig. 4 demonstrates two different steps of melting in typical particles of powder#2. Fig. 4(a) is a particle in the initial stage of melting, with a large proportion of unmolten particulates with distinct color of each component (white zirconia and black alumina). It is expected that such partly melted particles will preferably solidify in a crystalline structure which follows the structure of the original powder,[15] because of the presence of unmolten crystalline solids that play the role of nucleation sites for solidification. During heating and melting in the flame, the mixed region with grey color is readily developed in the particle observed in Fig. 4(b). The main difference between using systems 1 and 2 in the particles collected from powder#2 was that the number of well melted and mixed particles, as in Fig. 4(b), was greater when system 2 was used. Likewise, the observed change in the amorphous phase content in powder#3 sprayed by
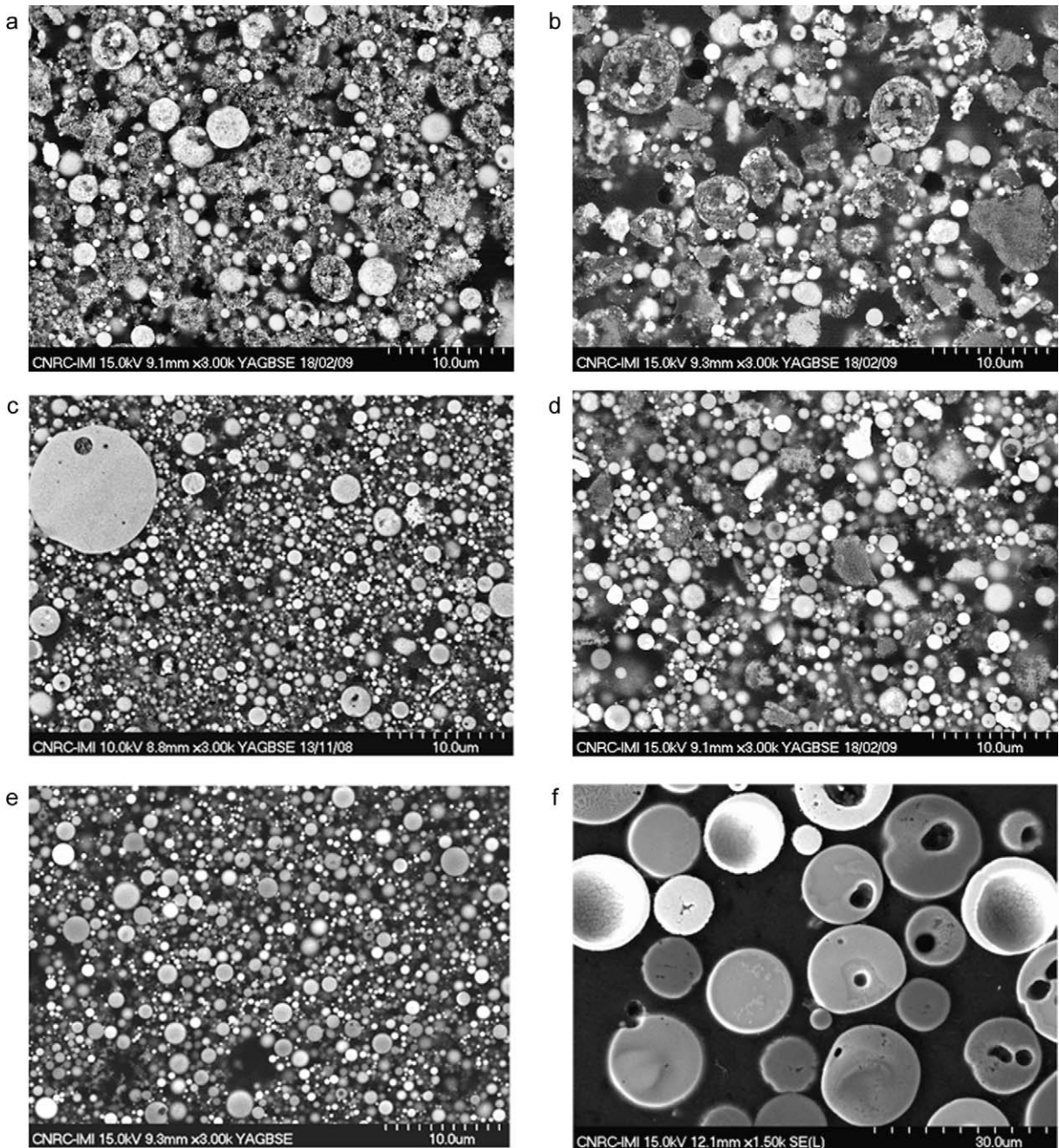
Fig. 3. SEM micrographs of the cross section of the in-flight particles collected in water, mounted and polished after spraying with SPS process (at 3000×) from (a) powder#1 (large agglomerated nano-particulates) using system 1; (b) powder#2 (loose nano-particles) sprayed using system 1; (c) powder#3 sprayed by system 1; (d) powder#2 sprayed using system 2; (e) the same as c, sprayed using system 2; (f) powder#1 sprayed by APS (at 1500×).

the two systems is found to be for the same reason, which is the different melting and mixing.

3.2. Collected powders in SPS and APS

Fig. 3(f), at 1500×, shows the collected powders after APS spraying of powder#1 and allows the comparison of the particle sizes resulting from spraying the same powder using the APS and SPS processes. It is evident that particles from the SPS process, as in Fig. 3(a), are much smaller than those formed in APS (average size of 1.6 μm from SPS compared with 45 μm from APS spraying of the same powder). It is noteworthy that the micrograph in Fig. 3(a) from SPS particles is at two times higher magnification than that of Fig. 3(f). Since the major difference between the two processes is the presence of a liquid carrier in SPS, the considerably smaller particle size can be mainly related to the presence of the liquid carrier helping deagglomeration of the large particles before and during spray process. This observation is compatible with the results of Chen et al.[17], where in HVOF deposition of the powder by liquid carrier process (solu-

Table 3
Spray conditions for suspension plasma spraying the coatings and the resulting in-flight particle characteristics at a spray distance of 50 mm.

Powder#	Plasma gas composition	Total plasma gas (slm)	Current (Amps)	Plasma power (kW)	Robot speed (m/s)	Number of passes	Injection system	Feed rate (kg/h)	Solid content (%)	$T_p \pm 30$ (°C)	$V_p \pm 10$ (m/s)	XRD calculated amorphous phase contents ±3% for coatings	Crystallization peak area of collected powders ±5% (arbitrary units)
1	Ar/N$_2$/He 75/10/15	245	200	61	80	35	1	1.8	30	2905	608	45%	12
2	Ar/N$_2$/He 75/10/15	245	200	61	80	35	1	1.8	30	–	630	25%	10
3	Ar/N$_2$/H$_2$ 65/15/20	275	240	114	40	26	1	1.8	30	3082	740[a]	11%	28
2	Ar/N$_2$/He 75/10/15	245	200	57	80	60	2	1.5	25	3080	612	36%	20[b]
3	Ar/N$_2$/H$_2$ 65/15/20	275	240	114	40	60	2	1.5	30	3080	612	48%	42[b]
4	Ar/N$_2$/H$_2$ 75/10/15	245	200	86	80	90	2	1.5	25	2950	640	–	–

[a] Particle velocity for the collected in-flight particles was different and equal to 698 m/s.
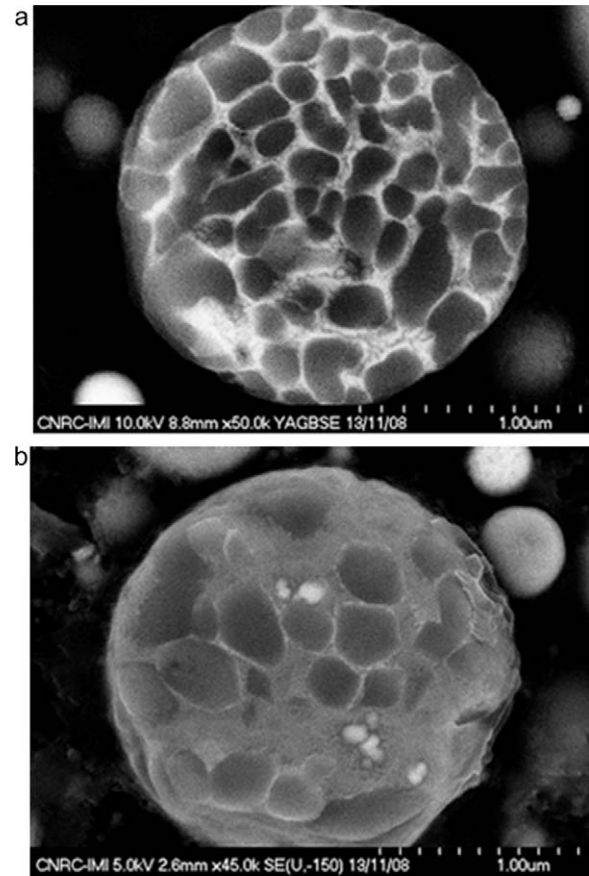[b] Calculated based on XRD results.[15]

Fig. 4. SPS-sprayed powder#1 (nano-agglomerated powder with initial structure shown elsewhere[18]) showing different stages of melting and mixing in the plasma jet: (a) partly melted with crystalline particles retained; (b) largely melted with extended mixing (grey color).

tion precursor high-velocity oxy-fuel spray), they observed ten times smaller splat sizes as compared with dry deposition using the same process. This means using the same powder, when employing the liquid precursor the resulting splat diameter was 2–5 μm while with dry deposition the splat sizes were in the range of 30–50 μm. The reason is known to be the significant in situ break-up of the liquid precursor and formation of small droplets in the high-velocity HVOF flame.[17] This explanation applies to SPS process as well. Such liquid break-up in dry deposition is not possible.

On the other hand, Fig. 5(a)–(c) illustrate various types of particles formed during spraying the nano-powders into water, which are observed in both sprayed powders either loose or agglomerated (powders#1 and 2), at high magnifications. In the comparison of the particles collected from SPS with those from APS process, as previously discussed,[16] there are some similarities, one of which is the presence of dendritic solidification in some particles. Examples can be found in Fig. 5(a) with fully dendritic structure and Fig. 5(b) that shows a partly mixed particle in which the dendrites are formed. These particles can be more frequently found among the particles sprayed with system 2 with higher melting proportions. Nevertheless, in the case of SPS particles, dendrite sizes are much smaller (less than 100 nm size) than what was found in APS-sprayed micron-particles.
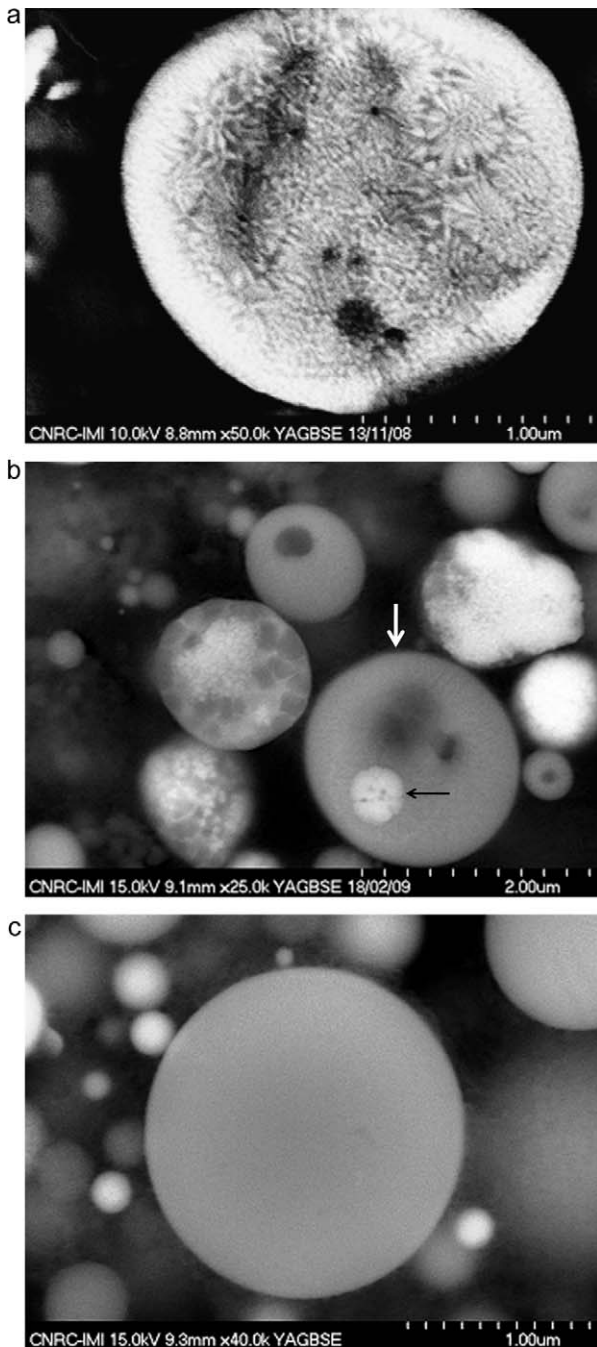
Fig. 5. SPS-sprayed powder#1 using spray system 1 collected in water: (a) fully dendritic growth in unmixed particles; (b) dendritic growth in partly mixed particle (arrowed); (c) non-crystalline particle.
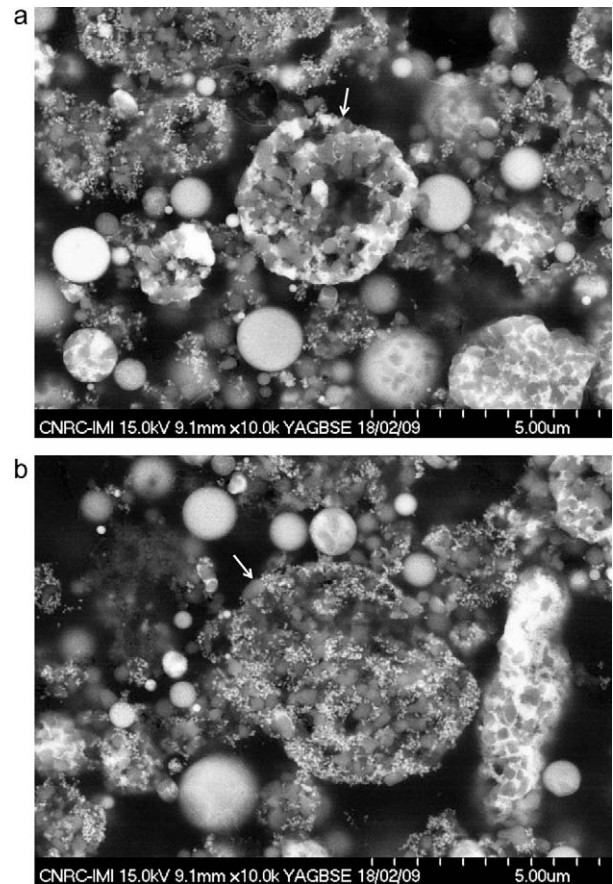

Fig. 6. Unmolten particles collected in-flight from SPS spraying of powder#1 using system 1: (a) partial segregation of components started; (b) no segregation accomplished.

In addition, particles with no sign of crystalline grains, as in Fig. 5(c), were found among SPS-sprayed particles as was previously observed in APS process. It is assumed here that these particles are the source of amorphous splats.

Conversely, particles with indications of eutectic or cellular crystallites, observed in APS-sprayed large particles,[16] were absent when spraying the small particles using SPS. The reason can be the invisibly small grain sizes within the small particles that are beyond the SEM capability. The absence of eutectic or cellular structure in the small particles (of SPS process) can

also be attributed to the extremely high cooling rates of small particles in SPS. Thus, if any mixing happens, the dense (no porosity) and extremely small particle (less than $2 \mu m$) tends to form amorphous phases instead of the crystalline phases that were found in the large and porous particles.[16] The formation of the crystalline structures with high dissolution of solute atoms can be confirmed from the XRD patterns. Indeed, in these patterns, peak shifting happens by solid solution formation in either zirconia or alumina crystals. Lattice parameters show the solid solubility variation in the crystalline solid. Such evaluation will follow later in this text.

Another difference between the APS and SPS sprayed powders is the segregation of the zirconia solid component outward the large unmolten particles of agglomerated powders. In SPS process, sometimes the segregation of dissimilar powder particles has also been observed, but to a very limited extent, as in Fig. 6(a). However, most of the particles have not encountered this, because of the short traveling path and high speed in SPS process; and they have maintained the initial form of the unmolten aggregates, shown in Fig. 6(b).

It should be noticed that in the coating samples some different trends may be expected than in the collected powders. Because, coatings are influenced by additional spray parameters such as number of deposition passes and spray robot speed.
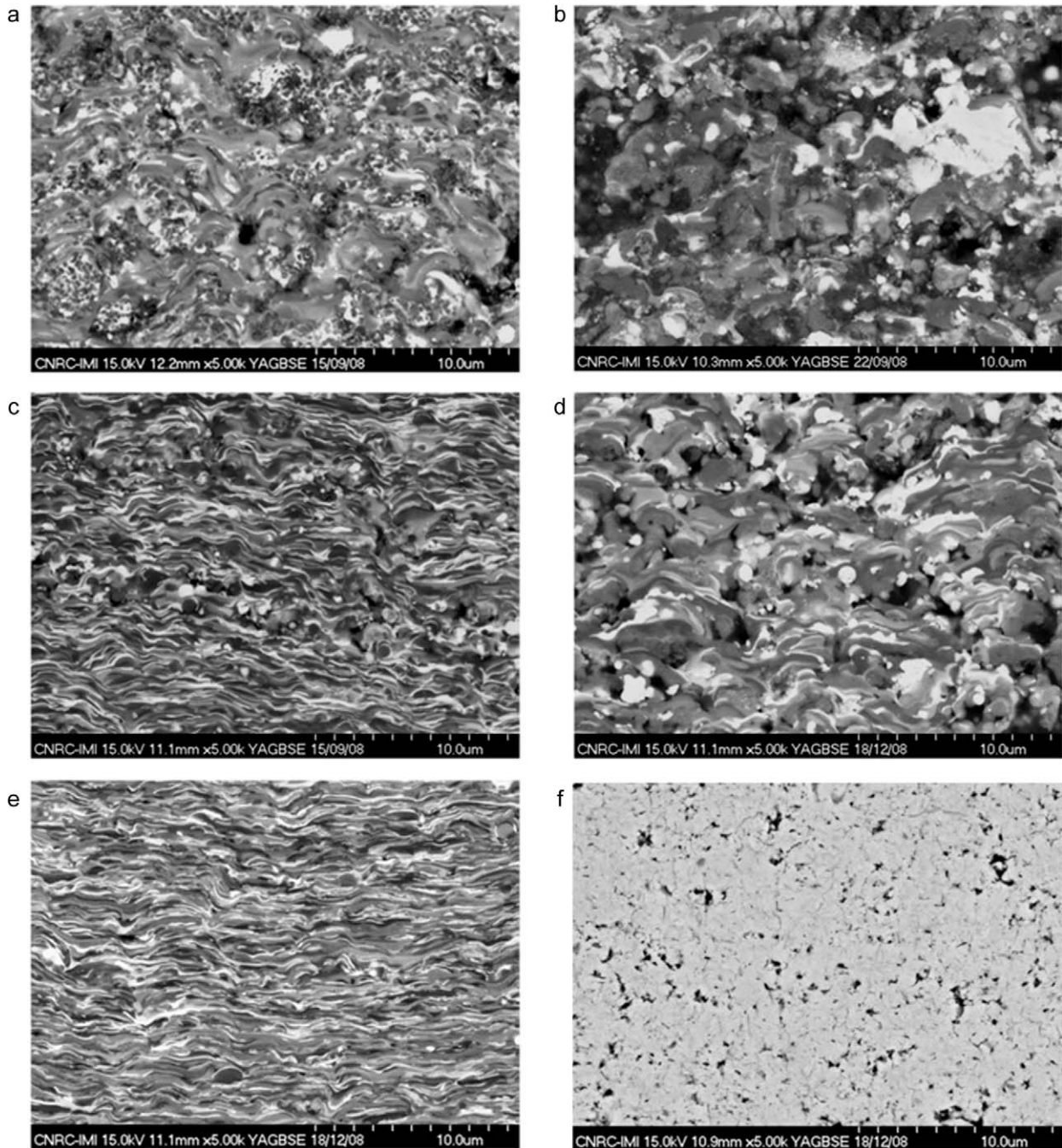
Fig. 7. SPS coatings from: (a) powder#1 sprayed with system 1; (b) powder#2 sprayed with system 1; (c) powder#3 sprayed with system 1; (d) same as b, sprayed with system 2; (e) same as c, sprayed with system 2; (f) 8 wt% YSZ nano-powder coated with system 2.

3.3. Coatings

The resulting coatings from the powders detailed in Table 1 and sprayed under conditions given in Table 3 can be compared in Fig. 7(a)–(e). In addition, Fig. 7(f) shows an 8 wt% YSZ (powder#4) coating deposited using system 2. This coating is produced for comparison of some properties of the materials used in this research with this most commonly used TBC.

Fig. 7(a) from powder#1 (agglomerated nano-particulates) deposited using system 1 presents a low fraction of molten par-

ticles. In this figure, the unmolten or partly molten particles are cemented in the fully molten splats forming a bi-modal structure (consisting of aggregates of unmolten nano-particles embedded in the molten and solidified structure), as found by Lima and Marple[18] in APS coating of 7 wt% YSZ. This coating consists of uniformly distributed phases within a continuous and sound microstructure. The molten part has formed a homogeneous structure, as observed in the non-crystalline particles of the collected powders. However, the present bi-modal structure consists of much smaller entities in terms of both splat size and unmolten particles than when APS was used.[18]
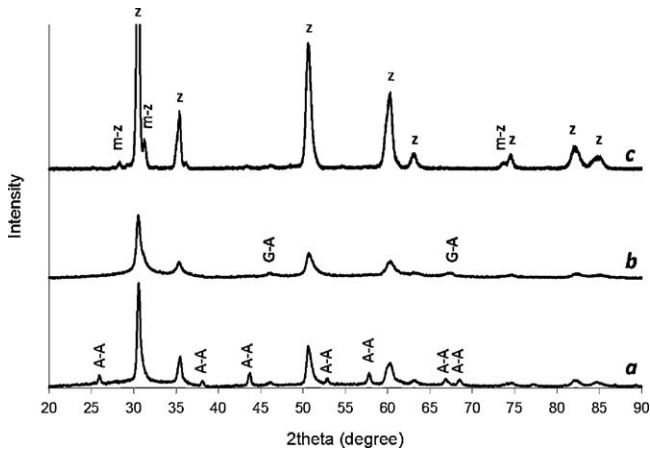
Fig. 8. XRD pattern of: (a) typical pattern of the coatings sprayed with system 1 (similar for four different coatings); (b) coating of powder#3 deposited with system 2 (the coating of exception); (c) coating of nano-powder of 8 wt% YSZ; where z represents the cubic (or t') zirconia, m-z is monoclinic zirconia, G-A shows γ alumina peaks and A-A is α-alumina.

Coatings from powder#2 (loose nano-powders) sprayed using system 1 are shown in Fig. 7(b). In spite of continuity, these coatings possess very loose intersplat connections of dissimilar splats with irregular boundaries and low mixing proportions. The coating in Fig. 7(d), using the same powder applied with system 2, in spite of the better melting conditions still lacks well-bonded splats. This is mainly because of the large fraction of partly molten particles observed in the corresponding collected particles in Fig. 4(a). The coatings from micron-powders in Fig. 7(c) and (e) suggest that when system 2 is used melting and splat flattening are improved.

The calculated amorphous contents for the coatings, as summarized in Table 3, show that, as a result of improved melting in powder#2 with system 2, the amorphous content has increased from 25% to 36%. For the coatings of powder#3, this phase shows a considerable increase from 11% to 48% with systems 1 and 2, respectively. Therefore it can be concluded that particles with full melting and mixing, and negligible or no retained unmolten solid, posses the best potential for amorphous formation within the coatings.

The monotonic structure of the 8 wt% YSZ deposited by SPS (Fig. 7(f)) presents porosity sizes from nano to a few microns. In addition, in this figure, no clear intersplat boundary can be found. This is in contrast with alumina–YSZ coatings shown in Fig. 7(a)–(e) with a large number of intersplat boundaries between the alumina and zirconia splats. This microstructural difference (apart from material dissimilarity) may result in differences in coating properties especially at high temperature which are the subject of future work.

3.4. Sources of crystalline phase and the nature of amorphous phase through XRD studies

The XRD patterns of the resulting coatings are shown in Fig. 8. These results suggest similar crystalline structures for the four coatings that consist of a combination of mainly cubic zirconia and (α + γ) alumina like in Fig. 8(a).
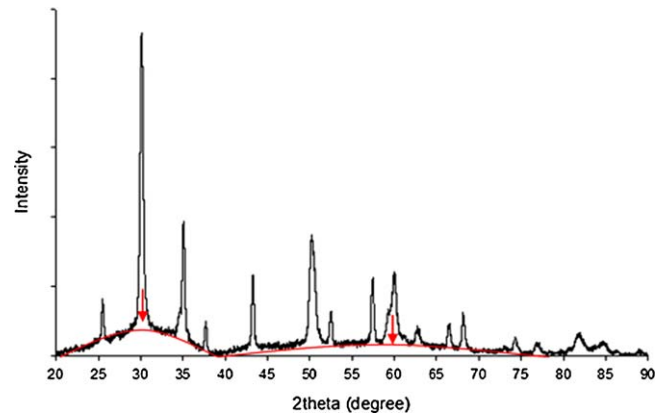

Fig. 9. XRD pattern of the coating of nano-powder 60 alumina-40 (8 wt% YSZ) deposited by SPS process using spray system 2, showing the location of amorphous hump mixima.

The exception is the coating shown in Fig. 8(b) that is for powder#3 (micron-powders) produced with system 2. This coating has the highest amorphous content (48% based on Table 3) and presents only γ-alumina with no α-alumina phase. This suggests the extensive melting resulting to disappearance of the initial α-alumina crystalline structure, and solidification at high cooling rates which favors γ-alumina phase formation.[15]

The structure of the nano-powder of 8 wt% YSZ (without alumina) deposited with SPS process, shown in Fig. 8(c), illustrates mainly cubic as well as some monoclinic zirconia in spite of the comparatively high content of yttria stabilizing agent. This structure is different from that found before,[16] where deposition of the same material using APS process results in mainly tetragonal structure. This difference can be explained by the high heat input from the torch to the substrate due to the short distance and much higher particle velocity and temperature found to influence phase formation as discussed elsewhere[17] encountered in the SPS process compared with APS, causing the formation of metastable phases.

The sources for the crystalline structures in the composite coatings, other than unmolten particles, can be the discrete splats of the unmixed material that tend to solidify in crystalline form rather than amorphous. Nevertheless, at extremely high cooling rates alumina splats on mild steel substrate interfaces have presented a very limited amorphous phase.[19] The other possibility reported in APS deposition of this composite, as detailed before,[14] is the solid solution formation. To investigate the formation of such crystalline solid solutions, the lattice parameters of various phases were obtained using structural refinement of the patterns based on Rietveld refinement method.[20]

The amorphous humps in these patterns are apparent in Fig. 9, which shows the XRD pattern of the coating of nano-powder deposited using system 2. They are centered at angles of about 30° and 57° that are the locations of the maximum intensity peaks for zirconia and the second maximum (91% intensity) of α-alumina, respectively. It is known that the maxima of the amorphous humps of each material are located at diffraction angles

where the peaks with maximum intensity of its crystalline structure occurs.[21] Therefore, these locations of amorphous hump peaks imply that the amorphous phase within the coating is parented by zirconia and/or alumina. It is noticeable that the first maximum of α-alumina (at 35°) is overlapping with the first zirconia hump.

It is known that the variation in lattice parameters of solid solutions represent the variation in the concentration of the solute atoms.[22] On the other hand, it can be presumed that the amount of amorphous phase is directly related to the mixing proportion. Therefore, an assessment of the changes in lattice parameters among the coatings with various amorphous contents has been performed. This is to find out if the solubility, measured by lattice parameter, is related to the amorphous content resulting from extensive mixing. The relationships between the amorphous content and the lattice dimensions in the crystalline portion of the coatings are depicted in Fig. 10.

Fig. 10(a) demonstrates the variations of parameter a for the cubic lattice of zirconia with the amount of amorphous phase. It shows that by increasing the amorphous content as a result of improved mixing, the lattice parameter of cubic zirconia increases. This suggests the enhancement of dissolution of the solute atoms in the crystalline structure of stabilized zirconia. The horizontal line in this figure represents the lattice parameter ($a = 5.1177$ Å) of the stabilized zirconia with no alumina added deposited under the conditions mentioned in Table 3. It can be seen that at lower amorphous content that can be translated to less dissolution, the lattice parameter is smaller than YSZ. However, at high dissolution ratios, it grows beyond the YSZ (with no dissolved alumina). This can be explained by changes in solute atom position in the lattice. Thus, when the aluminum takes the substitutional positions of the YSZ crystal, it causes the lattice to shrink. At higher amounts of dissolution, considering the much smaller radius of the aluminum (1.18 Å) atoms than zirconium (2.06 Å) and yttrium (2.12 Å), the zirconia structure may choose the interstitial positions for the solute to reduce the distortion and the related strain energy. Thus, allocation of the remaining aluminum atoms in the interstitial position results in expansion of the lattice.

Assessment of the α-alumina structure with the two parameters a and c reveals that the same approximate increasing trend is followed, as is apparent in Fig. 10(b) and (c). This means increased amorphous percentage is concurrent with the larger lattice parameter as a result of extended solubility. Zirconium atoms with a much larger atomic radius than aluminum cause the expansion of the alumina lattices by forming substitutional solid solution. This solubility sometimes is found to be as high as supersaturation.[16] Thus, the disappearance of the alumina component when sprayed with zirconia is attributed to two sources: the amorphous phase formation and the extended solid solubility into zirconia during plasma spray deposition. However, the large atomic number difference between aluminum and zirconium that can shadow the detection of small amounts of free crystalline alumina by XRD should not be ignored.[22] This means that small amounts of crystalline alumina in the system may exist, but due to low intensity of the scattered beams of aluminum, compared with zirconium and yttrium atoms are not detected.
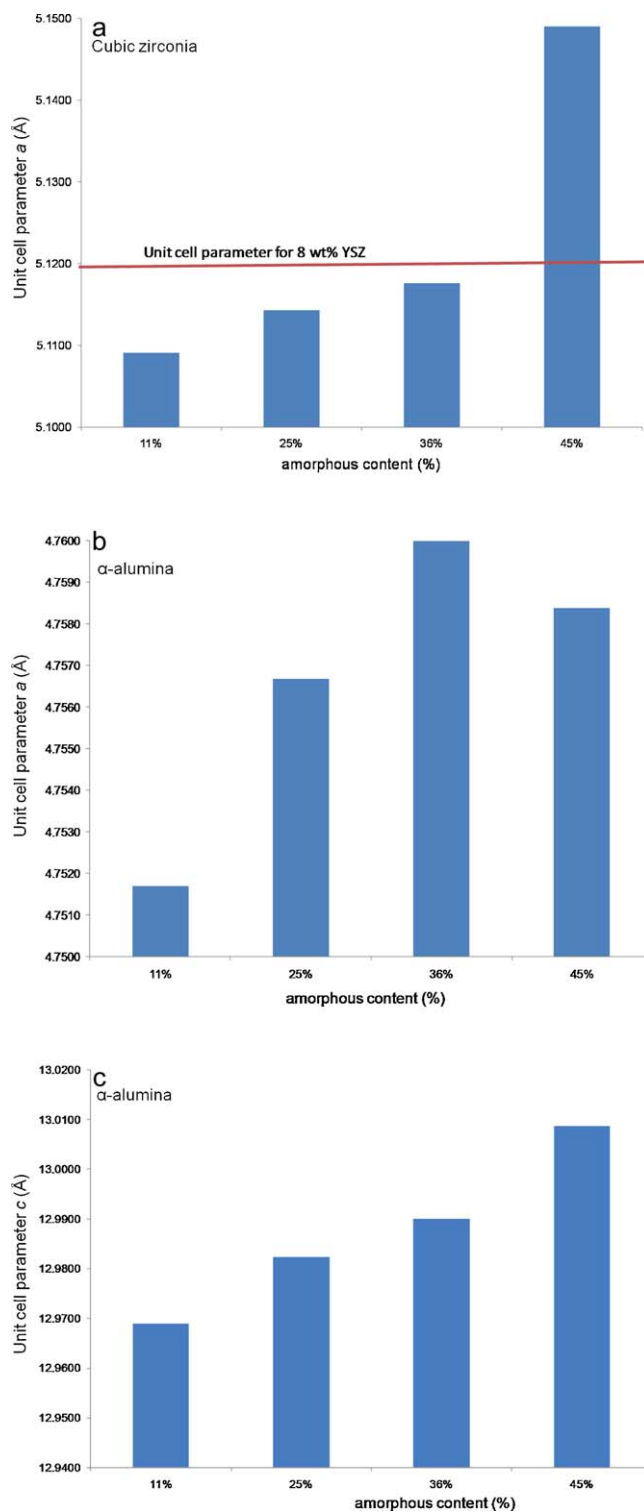

Fig. 10. Lattice parameters of the crystalline portion of the 60 alumina-40 (8 wt% YSZ) coatings (a) parameter a for cubic zirconia, (b) parameter a for α-alumina and (c) parameter c for α-alumina.

4. Conclusion

The in-flight collected particles studies suggest that there are major similarities between APS and SPS processes in terms of melting, mixing and phase formation as well as the effective

parameters on these phenomena. As a result, both methods can be used in the production of high amorphous coatings provided that the appropriate parameters for each process are utilized. However, the fragmentation of the nano-agglomerated particles in APS is negligible as compared with SPS and the dendrite sizes formed in APS process are clearly larger than what is formed in SPS in-flight solidified particles.

It is revealed that in-flight melting followed by mixing are crucial processes in amorphous formation. The observed role of the lower particle velocity that results in higher amorphous content, in spite of the lower cooling rates, is justified. This means that the significance of the in-flight particle velocity is due to its effect on longer times for melting and mixing. The amorphous phase in the coating seems to be composed of two compositional ranges, one with high alumina and the other with high zirconia. This was concluded from the amorphous humps maxima which match the locations of the main crystalline peaks of alumina and zirconia.

On the other hand, the crystalline structures present an exceptionally extended solubility of both components, especially alumina into the zirconia lattice. The lattice parameters studies suggest that the aluminum atoms possibly take the substitutional sites at low ratios and interstitial sites when higher amounts of alumina are being dissolved in zirconia. In contrast, large zirconium atoms have no choice but substitutional positions during dissolution in alumina structure, resulting in ever increasing the lattice parameters of alumina by dissolution ratio. The components in the composite materials sprayed by plasma processes may appear in different forms. They may form crystalline structure of alumina or YSZ with no additional solute atoms. They also can dissolve the solute atoms of the second component and form crystalline solid solutions (even to exceptionally high levels of solubility), and/or form amorphous phase.

Acknowledgement

References

1. Ramaswamy P, Seetharamu S, Varma KBR, Rao KJ. Al_2O_3–ZrO_2 composite coatings for thermal-barrier applications. *Composites Science and Technology* 1997;**57**:81–9.
2. Chen WR, Wu X, Dudzinski D, Patnaik PC. Modification of oxide layer in plasma-sprayed thermal barrier coatings. *Surface and Coatings Technology* 2006;**200**:5863–8.
3. Jayaram V, Levie CG, Whitney T, Mehrabian R. Characterization of Al_2O_3–ZrO_2 powders produced by electrohydrodynamic atomization. *Materials Science and Engineering A* 1990;**124**:65–81.
4. Chraska T, Neufuss K, Dubský J, Ctibor P, Rohan P. Fabrication of bulk nanocrystalline alumina–zirconia materials. *Ceramics International* 2008;**34**:1229–36.
5. Fauchais P, Vardelle M, Vardelle A, Bianchi L, Leger AC. Parameters controlling the generation and properties of plasma spray zirconia coatings. *Plasma Chemistry and Plasma Processing* 1996;**16**:99S–125S.
6. McDonald A, Chandra S, Moreau C. Photographing impact of plasma-sprayed particles on rough substrates. *Journal of Materials Science* 2008;**43**:4631–43.
7. McDonald A, Moreau C, Chandra S. Effect of substrate oxidation on spreading of plasma-sprayed nickel on stainless steel. *Surface & Coatings Technology* 2007;**202**:23–33.
8. Kim H-J, Kim YJ. Amorphous phase formation of the pseudo-binary Al_2O_3–ZrO_2 alloy during plasma spray processing. *Journal of Materials Science* 1999;**34**:29–33.
9. Chraska T, Neufussa K, Dubskya J, Ctibora P, Rohan P. Fabrication of bulk nanocrystalline alumina–zirconia materials. *Ceramics International* 2008;**34**:1229–36.
10. Sodeoka S, Suzuki M, Inoue T. Thermal stability and mechanical properties of plasma sprayed Al_2O_3/ZrO_2 nano-composite coating. *Key Engineering Materials* 2006;**317–318**:513–6.
11. Vasiliev AL, Padture NP. Coatings of metastable ceramics deposited by solution-precursor plasma spray: II. Ternary ZrO_2–Y_2O_3–Al_2O_3 system. *Acta Materialia* 2006;**54**:4921–8.
12. Vasiliev AL, Padture NP, Ma X. Coatings of metastable ceramics deposited by solution-precursor plasma spray: I. Binary ZrO_2–Al_2O_3 system. *Acta Materialia* 2006;**54**:4913–20.
13. Oberste-Berghaus J, Legoux J-G, Moreau C, Tarasi F, Chraska T. Mechanical and thermal transport properties of suspension thermal sprayed alumina–zirconia composite coatings. *Journal of Thermal Spray Technology* 2008;**17**:91–104.
14. Tarasi F. Suspension plasma sprayed alumina–yttria stabilized zirconia nano-composite thermal barrier coatings—formation and roles of the amorphous phase, PhD thesis, Concordia University, Montreal, Canada; 2010, 15.
15. Tarasi F, Medraj M, Dolatabadi A, Oberste-Berghaus J, Moreau C. Phase formation and transformation in alumina/YSZ nanocomposite coating deposited by suspension plasma spray process. *Journal of Thermal Spray Technology* 2010;**19**(4):787–95.
16. Tarasi F, Medraj M, Dolatabadi A, Oberste-Berghaus J, Moreau C. Structural considerations during atmospheric plasma spraying of the alumina-zirconia composite. *Surface & Coatings Technology* 2011, in press, doi:10.1016/j.surfcoat.2011.06.016.
17. Chen D, Jordan EH, Gell M. Solution precursor high-velocity oxy-fuel spray ceramic coatings. *Journal of the European Ceramic Society* 2009;**29**:3349–53.
18. Lima RS, Marple BR. Toward highly sintering-resistant nanostructured ZrO_2–7 wt.%Y_2O_3 coatings for TBC applications by employing differential sintering. *Journal of Thermal Spray Technology* 2008;**17**:846–52.
19. Chen HC, Pfender E, Dzur B, Nutsch G. Microstructural characterization of radio frequency and direct current plasma-sprayed Al_2O_3 coatings. *Journal of Thermal Spray Technology* 2000;**9**:264–73.
20. Manik SK, Dutta H, Pradhan SK. Microstructure characterization and phase transformation kinetics of polymorphic transformed ball milled a-TiO_2–10 mol% m-ZrO_2 mixture by Rietveld method. *Materials Chemistry and Physics* 2003;**82**:848–59.
21. Guinier A. *X-ray crystallographic technology*. London: Hilger and Watts Ltd.; 1952. pp. 330–176, 250–59, 282–84.
22. Cullity BD. *Structure of polycrystalline aggregates, in elements of X-ray diffraction*. 2nd ed. CA (USA): Addison-Wesley Publishing Company Inc.; 1978.